nature materials

Article

https://doi.org/10.1038/s41563-023-01473-9

Chiral-phonon-activated spin Seebeck effect

In the format provided by the authors and unedited

Contents

I. FILM CHARACTERIZATION

I.1. Measurements of circular dichroism spectrum of chiral-HOIP samples

Figure S1 shows the circular dichroism spectrum of representative hybrid organic-inorganic perovskite (HOIP) samples with chiral organic ligands. The opposite circular dichroism angles in the wavelength range of 300-600 nm validate the opposite chirality in the chiral-HOIP films.

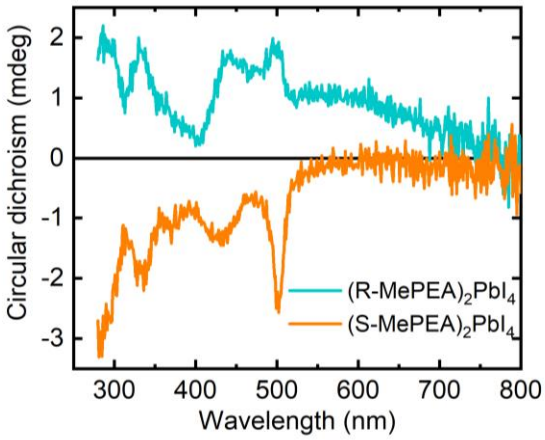

Fig. S1| The measured circular dichroism spectrum of (R-MePEA)$_2$PbI$_4$ and (S-MePEA)$_2$PbI$_4$.

I.2. X-ray diffraction (XRD) of the two-dimensional (2D) chiral HOIP films

Figure S2 shows the measured XRD results of the four 2D chiral HOIP films, which confirm the orientation of the prepared thin films, with the *c*-axis normal to the film surface. The positions of the first peak are different, which suggest different layer spacing between the inorganic layers in the 2D layered structure for these chiral HOIP films.

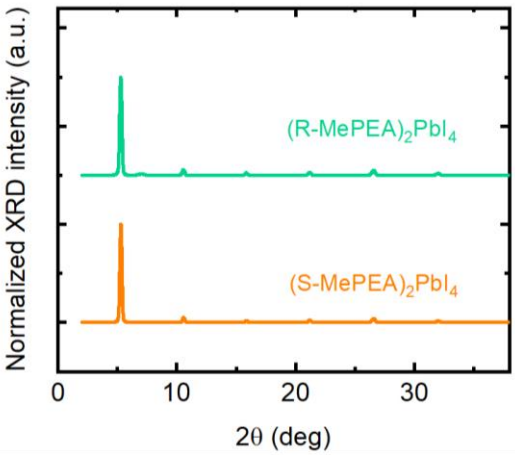

Fig. S2| The XRD spectrum of (R-MePEA)$_2$PbI$_4$ and (S-MePEA)$_2$PbI$_4$ films.

I.3. Atomic Force Microscope (AFM) scans of the sample surfaces

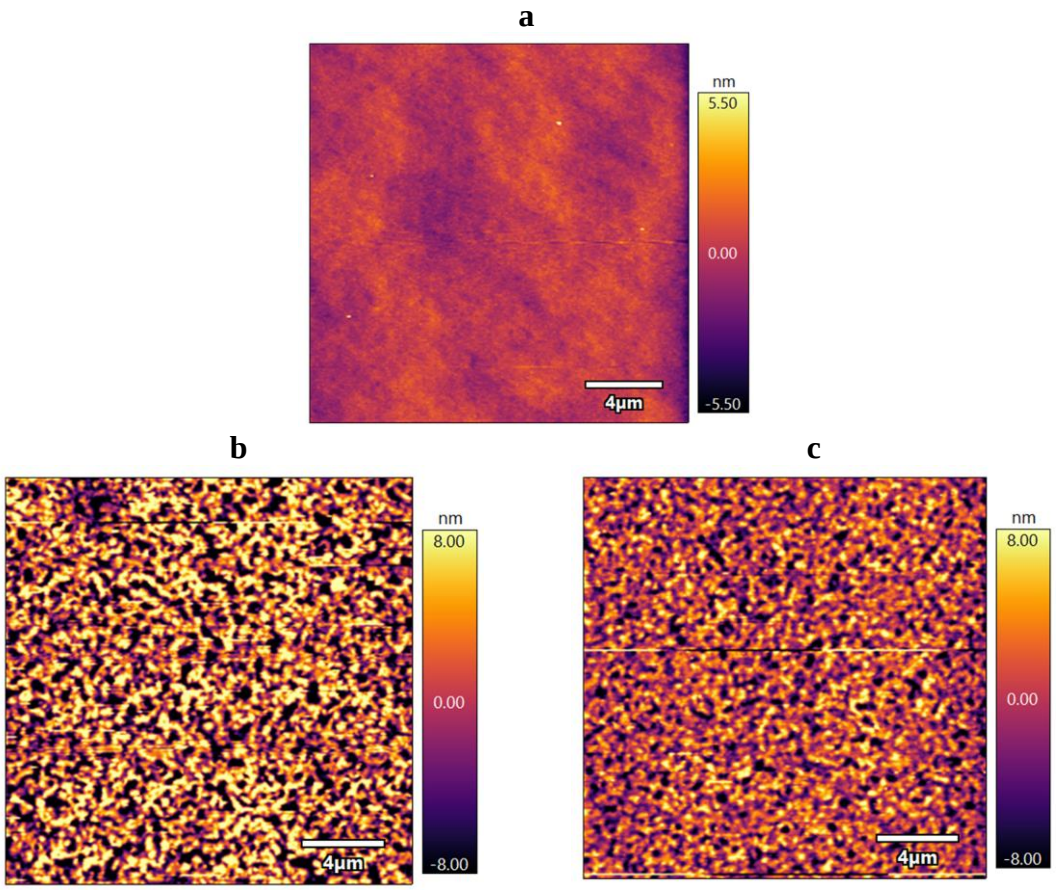

Fig. S3| AFM scans of the sample surfaces within a 20×20 μm^2 area. **a,** NiFe/Cu/SiO_2/Si. **b,** NiFe/Cu/(*S*-MePEA)$_2$$PbI_4$/Si. **c,** NiFe/Cu/(*R*-MePEA)$_2$$PbI_4$/Si.

Figure S3 shows the AFM images of the NiFe control sample (NiFe/Cu/SiO_2/Si), the Chiral-*S* sample (NiFe/Cu/(*S*-MePEA)$_2$$PbI_4$/Si), and the chiral-*R* sample (NiFe/Cu/(*R*-MePEA)$_2$$PbI_4$/Si). The surfaces of all three films are uniform and homogeneous. **Table S1** shows the R.M.S. surface roughness of the three samples. The surface of the chiral samples is relatively rougher compared to the control sample. All the three surfaces can be viewed as optically smooth surfaces (R.M.S. roughness<15 nm) for TRMOKE and TDTR measurements.

Table S1. The R.M.S. surface roughness in three samples.

Sample configuration	*R.M.S. surface roughness*
NiFe/Cu/SiO_2/Si	0.8 nm
NiFe/Cu/(S-MePEA)$_2$$PbI_4$/Si	7.4 nm
NiFe/Cu/(R-MePEA)$_2$$PbI_4$/Si	6.4 nm

II. CONTROL MEASUREMENT – SDSE IN METALLIC FILMS

II.1. Measurements of transient Kerr rotation signals on the Cu/Ni/SiO_2/Si control sample

We measured the transient Kerr rotation signals on the Cu (100 nm)/Ni (50 nm)/ SiO_2 (300 nm)/Si sample with an external 90 mT magnetic field. Ni is a ferromagnet with a low magnetization ~500 emu/cc,[1] which requires a relatively weak field of ~6.3 kOe to sufficiently tilt the magnetization out of the plane. Without an external magnetic field, the magnetization of the Ni film lies in the in-plane direction. With a strong external field of B=+90 mT (-90 mT), the direction of the magnetization of the Ni film is in the polar direction pointing outward (inward). When the Ni film is exposed to a transient temperature gradient across the film due to ultrafast laser heating (see the calculation of the temperature profile in **Fig. S11**), the ultrafast spin-dependent spin Seebeck effect (SDSE) will induce a transient spin current in the Ni film and flow into the Cu film.[2] When a probe beam measures the spin accumulation on the surface of the Cu film, the Kerr rotation signals would be either positive or negative, depending on the direction of the magnetization of the Ni film under the external magnetic fields. **Figure S4** shows the transient Kerr rotation signals when external magnetic fields with opposite polarities are applied to the sample. The sign of the peaks flips when the external magnetic field flips the polarity.

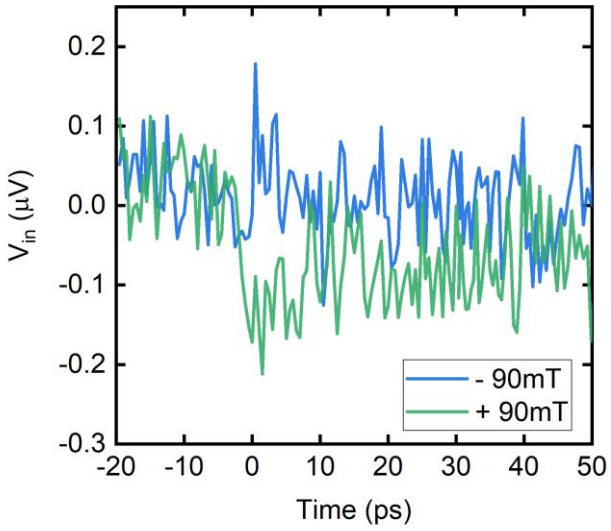

Fig. S4| Transient Kerr rotation signals on the Cu/Ni/SiO_2/Si sample with 90 mT external magnetic field.

III. DETERMINATION OF THERMAL PROPERTIES AND TEMPERATURE GRADIENTS ACROSS THE FILMS

III.1. Measurements of thermal conductivity and heat capacity of chiral films using the TDTR method

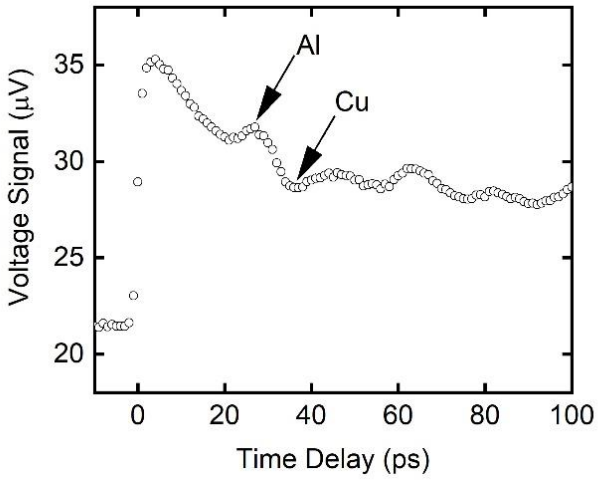

Fig. S5| The TDTR signal as a function of time delay in the short timescale (-20 ~100 ps) for determining the film thickness from acoustic echoes. This signal is measured on the Al/Cu/(R-MePEA)$_2$PbI$_4$/Si sample using a Gaussian spot size of 11 microns.

In the time-domain thermoreflectance (TDTR) method,[3,4] a mode-locked Ti:sapphire laser produces a train of pulses at a repetition rate of 80 MHz. A mechanical delay stage is used to change the optical path difference between the pump and probe before they are focused through an objective lens onto the sample surface. Prior to the TDTR measurements, ~80 nm Al thin films were deposited onto the samples by e-beam evaporation. The pump beam is modulated at a frequency *f* so that the thermoreflectance change at the sample surface can be detected by the probe beam through lock-in detection. More details on TDTR can be found in our previous publications.[5-8]

For the samples Al/Cu/Chiral/Si, the accurate thickness of Al and Cu films is determined by the acoustic echoes in the short timescale in the TDTR data (**Fig. S5**).

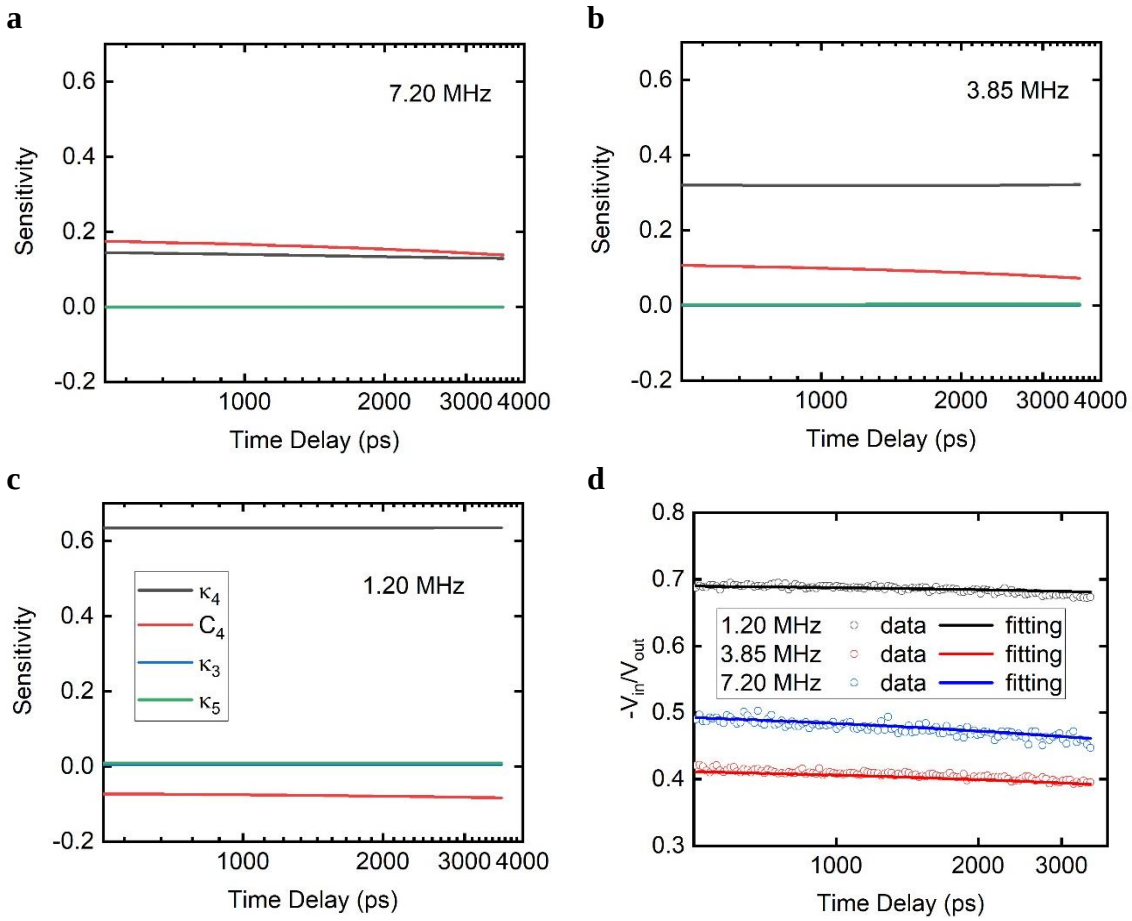

Fig. S6| The sensitivity analysis and the data fitting. The sensitivities of the measurement signals to the thermal conductivity of chiral film, κ_4, the volumetric heat capacity C_4, the interfacial thermal conductivity between Cu and chiral films, κ_3, the interfacial thermal conductivity between chiral films and Si substrate, κ_5, at a modulation frequency of **a,** 7.20 MHz, **b,** 3.85 MHz, and **c,** 1.20 MHz. **d,** The TDTR ratio data as a function of time delay (open circles) and fitting curves (solid lines).

We used frequency-dependent TDTR to measure both the thermal conductivity κ and heat capacity C of the chiral films.[6-8] This approach is based on the fact that the sensitivities of the measurement signal to κ and C vary differently with f. **Figure S6** shows the sensitivity analysis and the data fitting. At relatively high f, the film thickness d is much larger than the thermal penetration depth in the sample $L=\sqrt{k/\pi Cf}$ ($d>>L$); in this case, the thermal effusivitiy of the film $\sqrt{kC}$ governs the heat flow in the sample. **Figure S6a** demonstrates this case with the sensitivities of thermal conductivity and heat capacity similar to each other. At sufficiently low f, $d<<L$, the thermal resistance d/κ governs the heat flow in the sample and the signal is more sensitive to thermal conductivity and less sensitive to heat capacity. For intermediate modulation frequencies the sensitivity of the measurement signal to heat capacity cross through zero (**Figs. S6b** and **S6c**).

We measured thin chiral films at three modulation frequencies, 7.2 MHz, 3.85 MHz, and 1.2 MHz, with a Gaussian $1/e^2$ radius of the focused laser beams of 11 microns. For each sample, we simultaneously fit the TDTR ratio data at the three modulation frequencies to extract both thermal conductivity and volumetric heat capacity of the chiral thin films (**Fig. S6d**). In the fitting, the heat capacities of Al, Cu, and Si are adopted from the literature values.[9] The thickness of Al and Cu thin film was obtained from the picosecond acoustics. The thermal conductivity of the Al films is obtained by measuring the in-plane electrical conductivity on an insulating substrate and applying the Wiedemann-Franz law. **Table S2** shows the fitting parameters.

Table S2. Fitting parameters used to extract the thermal conductivity and volumetric heat capacity of chiral films.

Materials or interface	*Thickness (nm)*	*Thermal Conductivity (W/m-K)*	*Volumetric Heat Capacity (J/cm^3-K)*
Al	86.4	140	2.42[9]
Cu	23.0	110[10]	3.45[9]
Cu/Chiral	1	0.1	0.1
Chiral	156	**0.13**	**1.42**
Chiral/Si	1	0.1	0.1
Si	5×10^5	140	1.6[9]

To validate our measurement approach, a ~100 nm-thick poly(methyl methacrylate) (PMMA) film was spun-cast on a silicon substrate and measured using a similar approach. The best fit values are $\kappa = 0.18 \pm 0.02$ W m^{-1} K^{-1} and $C = 1.7 \pm 0.2$ J cm^{-3} K^{-1}, and the difference is within 5% as compared with the reported values of PMMA.[11,12] We have also used this approach to measure the thermal conductivity and heat capacity of PEDOT:PSS thin films.[8]

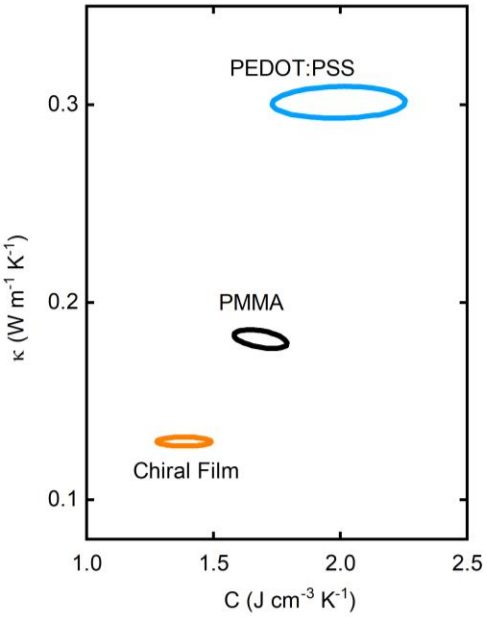

Fig. S7| Contour map derived from the goodness-of-fit for frequency-dependent TDTR data as a function of thermal conductivity κ and heat capacity *C* for chiral films. The measurements on the PMMA and PEDOT:PSS films are also plotted as references.

For the TDTR measurement of thermal conductivity and heat capacity of chiral films, we define a parameter ξ, as in our previous work in measuring organic thin films, to quantify the goodness-of-fit. The ξ is the sum of the standard deviation between the model prediction and measurement data at all three frequencies and delay times from 0.5 to 3.6 ns. **Figure S7** shows the contour of constant $\xi = 2\xi_{\min}$ (i.e., a 95% confidence level) as a function of thermal conductivity and heat capacity of PMMA, PEDOT:PSS, and chiral films. These uncertainties are determined by the signal-to-noise ratio of the measurement and the quality of the fit of the data to the thermal model. The total uncertainties of the measured thermal conductivity and heat capacity are calculated by adding these measurement uncertainties in quadrature with the systematic errors that propagate from uncertainties in the film thickness, laser spot size, and thermal properties of the transducer film and substrate.

III.2. Determine the temperature profile and temperature gradient inside the chiral films

To solve the d.c. and a.c. temperature profile and temperature gradient inside the chiral films, we made an in-house code to numerically solve the time-dependent temperature response in the multilayer material upon periodic ultra-short pulsed laser heating. To balance the computational accuracy and efficiency, we adopted a cylindrical coordinate system with only two variables: *r*, which is the along the Gaussian beam radial direction, and *z*, which is along the through-thickness direction. For metallic layers, such as Cu and Ni, a two-temperature model is employed to describe the heat transfer non-equilibrium between phonons and electrons. For other

layers, only phonons are considered for heat transfer. The initial temperature in the system is set as 300 K. The evolution of temperature in the multi-layer material at different time can be calculated according to the following heat conduction equations. For heat transfer with phonons only:

$$C_p(T_p)\frac{\partial T_p}{\partial t} = -\nabla \cdot \boldsymbol{J}_{p,E}. \quad \text{(Eq. S1)}$$

For metals, the heat conduction equation with two-temperature model is:[13]

$$C_e(T_e)\frac{\partial T_e}{\partial t} = -\nabla \cdot \boldsymbol{J}_{e,E} - G(T_e - T_p) + Q(\boldsymbol{r}, t), \quad \text{(Eq. S2)}$$

$$C_p(T_p)\frac{\partial T_p}{\partial t} = -\nabla \cdot \boldsymbol{J}_{p,E} + G(T_e - T_p). \quad \text{(Eq. S3)}$$

Here $C_e(T_e)$ and $C_p(T_p)$ is the electronic and lattice heat capacity, $\boldsymbol{J}_{e,E}$ and $\boldsymbol{J}_{p,E}$ are the energy current densities of electrons and phonons, respectively. The two-temperature model follows closely the Fourier's law of heat conduction $\boldsymbol{J}_{e,E} = -\kappa_e(T_e, T_p)\nabla T_e$ and $\boldsymbol{J}_{p,E} = -\kappa_p(T_p)\nabla T_p$, where $\kappa_e(T_e, T_p)$ is the electronic thermal conductivity and $\kappa_p(T_p)$ is the lattice thermal conductivity. In particular, the ultra-short pulse laser is used for heating and its energy is absorbed by electrons in the top metallic layer. Therefore, for the top metallic layer, an energy term $Q(\boldsymbol{r}, t)$ from the pulse laser needs to be considered in the electron heat conduction equation, and the energy deposition form is as follows:[13]

$$q(r,z,t) = \frac{2}{\pi w^2}\exp\left[-2\frac{r^2}{w^2}\right]\left[P_0 + P_0\sin(\omega_0 t)\right]\left[\frac{0.94}{f_{rep}\tau_p}\sum_{-\infty}^{\infty}\exp(-2.77\frac{(t-nT_s)^2}{\tau_p^2})\right]\frac{1}{\delta}\exp(-\frac{z}{\delta})\frac{1}{1-\exp(-L/\delta)}, \quad \text{(Eq. S4)}$$

where the absorbed power P_0 is

$$P_0 = P \times (1-R). \quad \text{(Eq. S5)}$$

All the symbols are defined in **Table 3**. Because the duty cycle in the ultra-short pulse laser is large, and the electronic energy in the top metallic layer changes significantly with the incidence of pulsed laser, it needs to be handled carefully. Thus, for the layer with or without direct laser incidence, we used the Runge-Kutta algorithm of the medium order method (ode45) and the variable order method (ode15s), respectively, to achieve a balance between computational accuracy and efficiency. In this calculation, we consider the influence of the heat transfer process of both electrons and phonons in the metals and the interfacial thermal resistance, with detailed parameters shown in **Table S3**. After a sufficiently long time, the temperature in the multilayer material system will reach a steady state. The a.c. and d.c. temperature profile can be extracted by fast Fourier transform at the steady state.

Table S3. Summary of the thermal properties of materials and properties of ultrafast laser used in the simulation.

Thermal Properties of Materials[9,14]			
Cu electronic heat capacity	0.021 J/cm^{3}K	Cu phononic heat capacity	3.43 J/cm^{3}K
Cu electronic thermal conductivity	300 W/mK	Cu phononic thermal conductivity	12 W/mK
Cu electron-phonon coupling	4.8×10^{16} W/m^{3}K	Cu/Chiral interface	100 MW/m^{2}K
Chiral thermal conductivity	0.13 W/mK	Chiral heat capacity	1.42 J/cm^{3}K
Chiral/Si interface	100 MW/m^{2}K	Si thermal conductivity	140 W/mK
Si heat capacity	1.6 J/cm^{3}K	Cu/Ni interface phonon contribution	1 GW/m^{2}K
Cu/Ni interface electronic contribution	40 GW/m^{2}K	Ni electronic heat capacity	0.323 J/cm^{3}K
Ni phononic heat capacity	3.593 J/cm^{3}K	Ni electronic thermal conductivity	84 W/mK
Ni phononic thermal conductivity	15 W/mK	Ni electron-phonon coupling	105×10^{16} W/m^{3}K
Ni/SiO_2 interface	100 MW/m^{2}K	SiO_2 heat capacity	1.67 J/cm^{3}K
SiO_2 thermal conductivity	1.35 W/mK	SiO_2/Si interface	500 MW/m^{2}K
Properties of Ultrafast Laser			
Pulse width τ_p	0.25 ps	Repetition rate f_{rep}	80 MHz
Laser spot size w	6 μm	Surface reflectivity R *(Cu)*	0.96
Optical penetration depth δ *(Cu)*	12.8 nm[15]	Surface reflectivity R (*NiFe*)	0.667
Optical penetration depth δ *(NiFe)*	13.8 nm	Modulation frequency ω_0	1.0 -10 MHz
Incident power P	10-40 mW	Repetition time T_s	12.5 ns

Here we show transient temperature response, d.c./a.c. temperature rises, and temperature gradient in representative chiral and control samples. **Figure S8** shows the transient temperature response at different time scales after the first laser pulse on a typical sample. **Figure S8a** shows the overview where the temperature response can be divided into two parts: the d.c. and a.c. temperature rises. The d.c. temperature rise is due to the temperature accumulation in the sample: the heat dissipation after the sample being heated by the laser pulse is typically much longer than the short time (12.5 ns) between laser pulses. The a.c. temperature rise is due to the periodic modulated heating. The expanded view of the temperature response in **Figs. S8b and S8c** shows the transient response after each pulse heats the sample surface initially and after reaching a steady state.

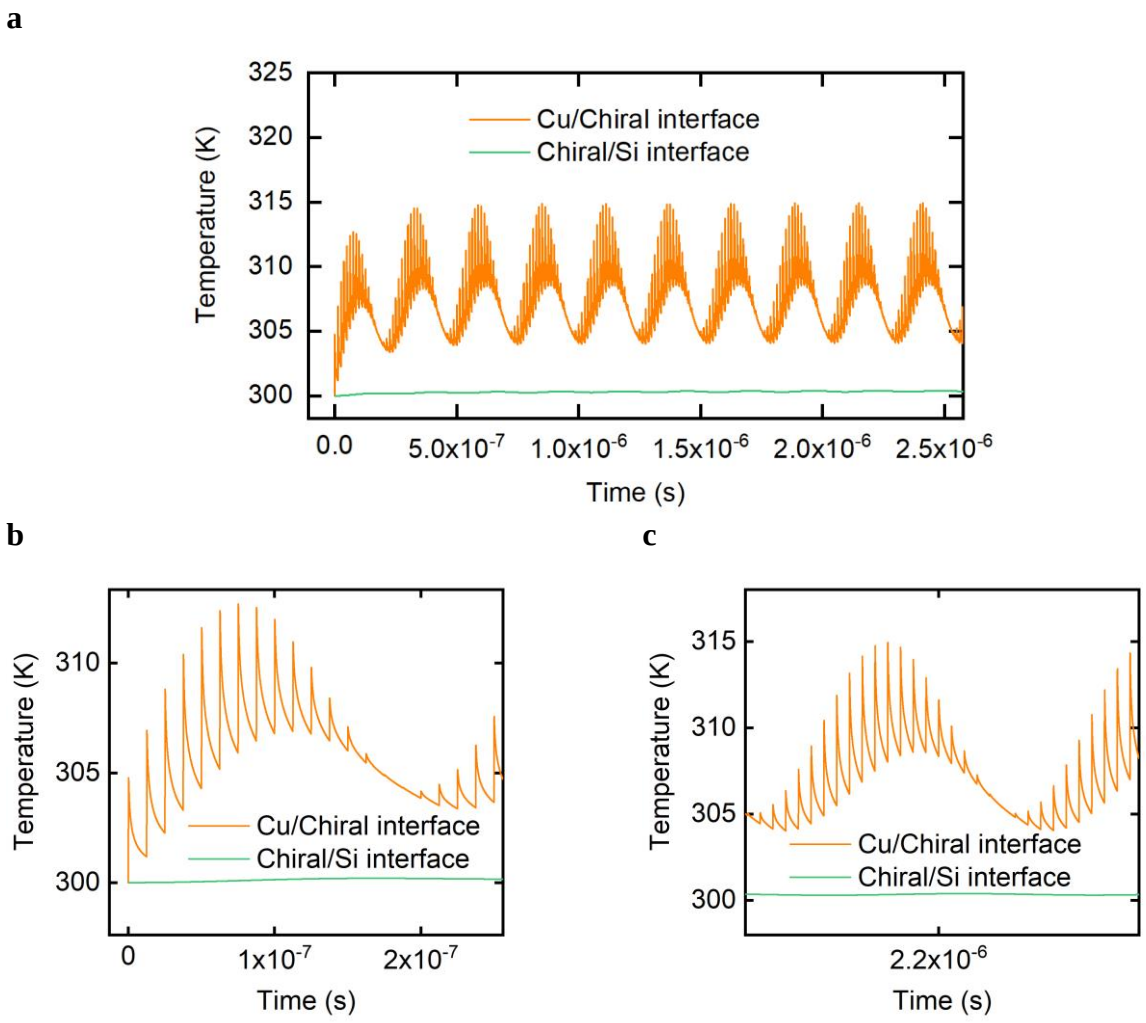

Fig. S8| Transient temperature response in the Cu/Chiral and Chiral/Si interface in the 15 nm NiFe/50 nm Cu/150 nm Chiral/Si sample. The effective incident power is 32 mW and the modulation frequency of the pump beam is 3.85 MHz. **a,** The overview of the temperature response from t=0 to 2.5 μs. The temperature response can be divided into two parts: a DC temperature rise due to the accumulated heating in the sample and an AC temperature rise due to the periodic pulse heating. **b,** The initial temperature response from t=0 to 0.25 μs. **c,** The temperature response after the sample has reached a steady state.

Figure S9 shows the d.c. and a.c. temperature profiles in the samples 15 nm NiFe/50 nm Cu/150 nm Chiral S(or R)/Si at an incident power of 32 mW and three modulation frequencies of 1.0 MHz, 4.0 MHz, and 10.0 MHz. The d.c. temperature rise is much higher than the a.c. temperature rise in the samples. The thermal penetration depth into the chiral film is much shorter at a higher modulation frequency.

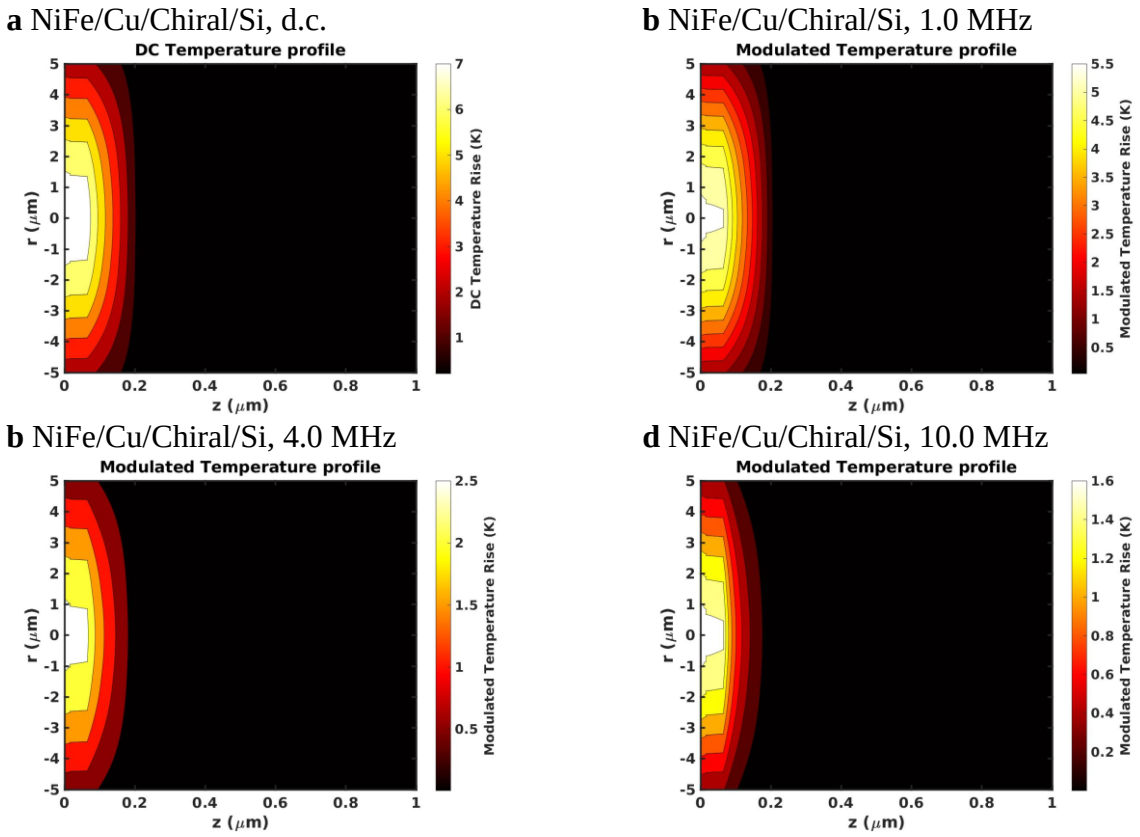

Fig. S9| Temperature profile in NiFe/Cu/Chiral S(or R)/Si when modulated ultrafast laser heats the surface. a, The d.c. temperature profile. **b,** 1.0 MHz modulated temperature profile. **c,** 4.0 MHz modulated temperature profile. **d,** 10.0 MHz modulated temperature profile.

Figure S10 shows the dependence of temperature gradient on the laser incidence power and modulation frequency of pump beam. The d.c. and a.c. temperatures are obtained by analyzing the steady-state temperatures. The temperature gradient is averaged by calculating the temperature difference within the thermal decay length, which represents a length scale where the temperature drops below 1/*e* (36.7%) of the surface temperature of the chiral film. The thermal decay length increases with decreasing modulation frequency. Both the a.c. and d.c. temperature gradient increases linearly with the incident power. The d.c. thermal gradient is independent of the modulation frequency. The a.c. thermal gradient is higher at the lower modulation frequency in both samples, about three times in 1 MHz compared to 10 MHz in the NiFe/Cu/Chiral S(or R)/Si sample.

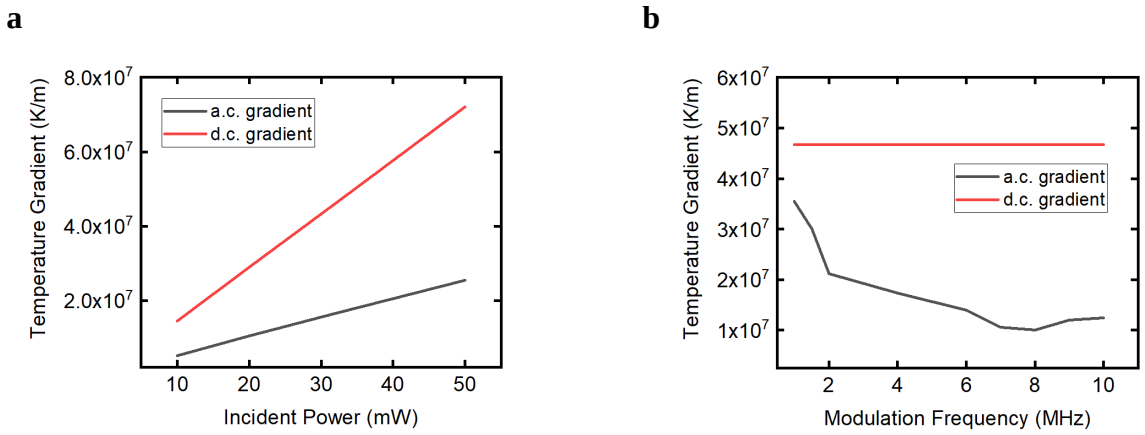

Fig. S10| Dependence of the temperature gradient across the chiral film on the incident power and modulation frequency of pump laser in the sample 15 nm NiFe/ 50 nm Cu/ 150 Chiral S(or R) film/Si. a, Temperature gradient across the chiral film as a function of incident power at a modulation frequency of 3.85 MHz. **b,** Temperature gradient across the chiral film as a function of modulation frequency when the incident power is 32 mW.

Figure S11 shows the transient temperature response in Cu/Ni/SiO_2/Si sample after reaching the steady state at a modulation frequency of 7.2 MHz and an incident power of 30 mW. The solution considers both phonons and electrons in the Cu and Ni layers. At the first 100 ps after each pulse, there is a temperature difference with the magnitude about 3-4 K across the 50 nm Ni film.

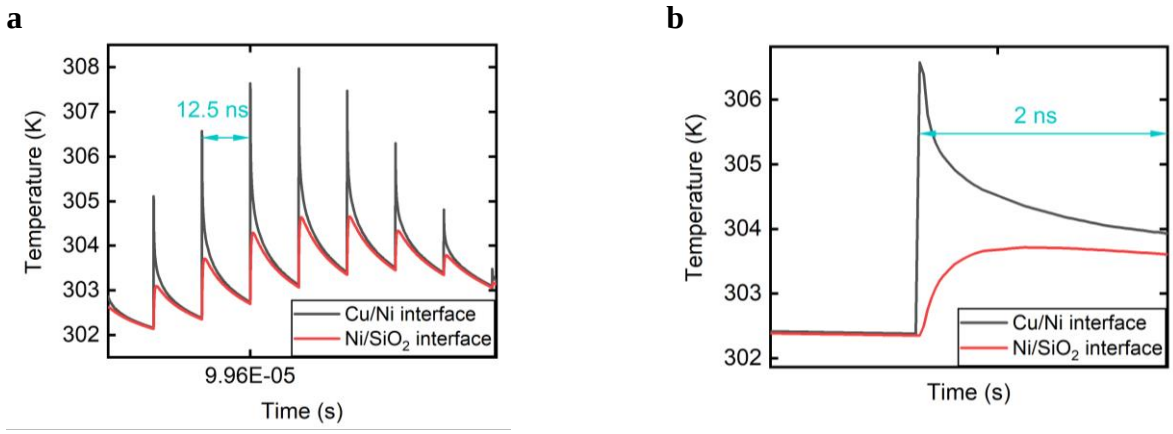

Fig. S11| The transient temperature response in Cu (100 nm)/Ni (50 nm)/ SiO_2 (300 nm)/Si sample. a, The view at a relatively longer time scale. **b,** The temperature response at the steady state at an expanded view.

IV. MAGNETIC DYNAMICS CHARACTERIZTION OF NIFE FILMS

IV.1. Magnetic hysteresis and *M* v.s. *H* loops on the control and chiral samples

We have measured the *M* v.s. *H* loop along with both the in-plane and out-of-plane field directions on the control sample (NiFe/Cu/Si) and R/S chiral films (NiFe/Cu/(*R*- or *S*-$(MePEA)_2PbI_4$)/Si) using the SQUID magnetometer. **Figures S12** and **S13** show the obtained *M* v.s. *H* loops along with the in-plane and out-of-plane external field directions at 300 K and 100 K, respectively.

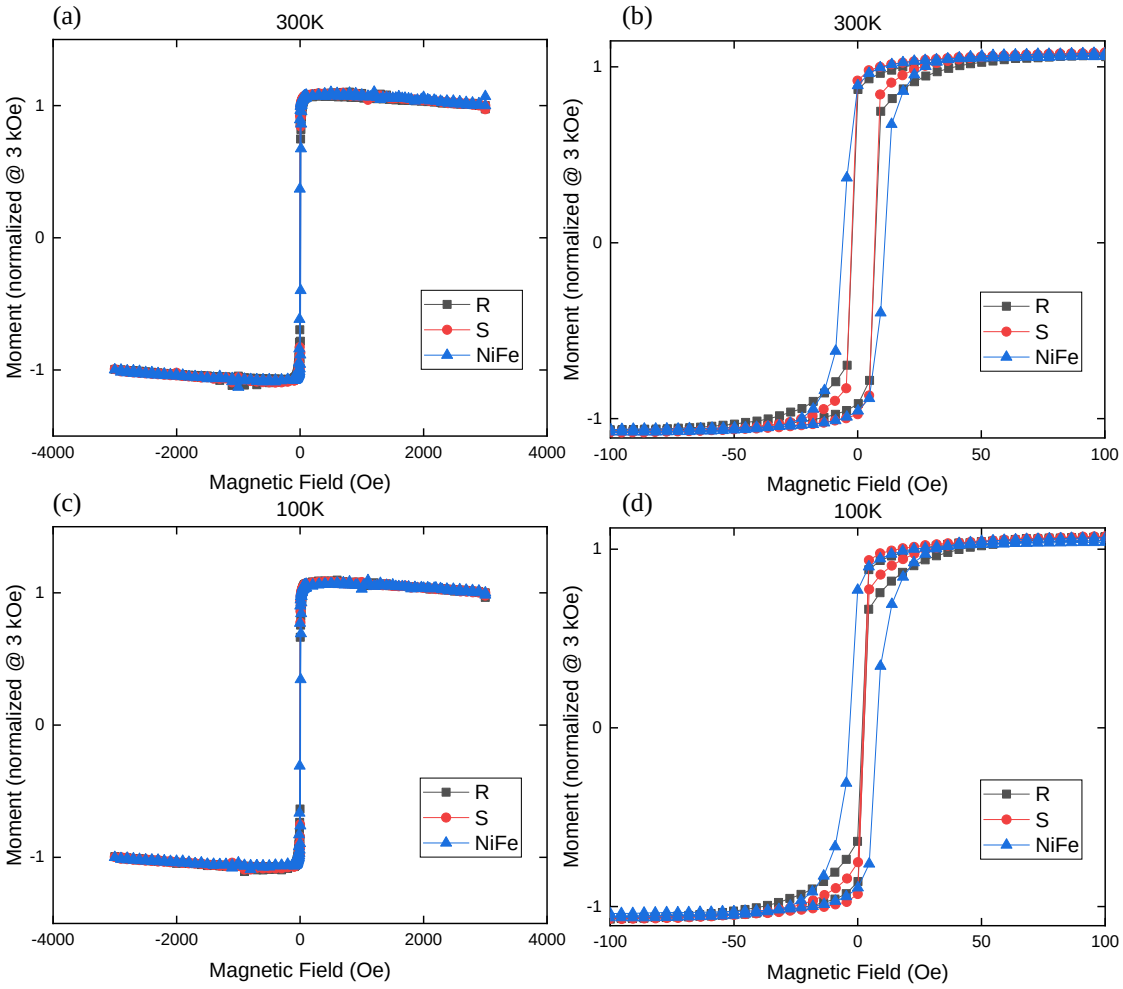

Fig. S12| The measured *M* v.s. *H* loops along with the in-plane external field direction on the control sample (NiFe/Cu/Si) and R/S chiral films (NiFe/Cu/(*R*- or *S*-$(MePEA)_2PbI_4$)/Si) at T=300 K **(a)** and 100 K **(c)**, respectively. **(b)** and **(d)** show the zoomed-in magnetic hysteresis loops within within ±100 Oe at both temperatures, respectively, showing no clear difference between three samples. The magnetic moment is normalized at the value at *H* = 3000 Oe.

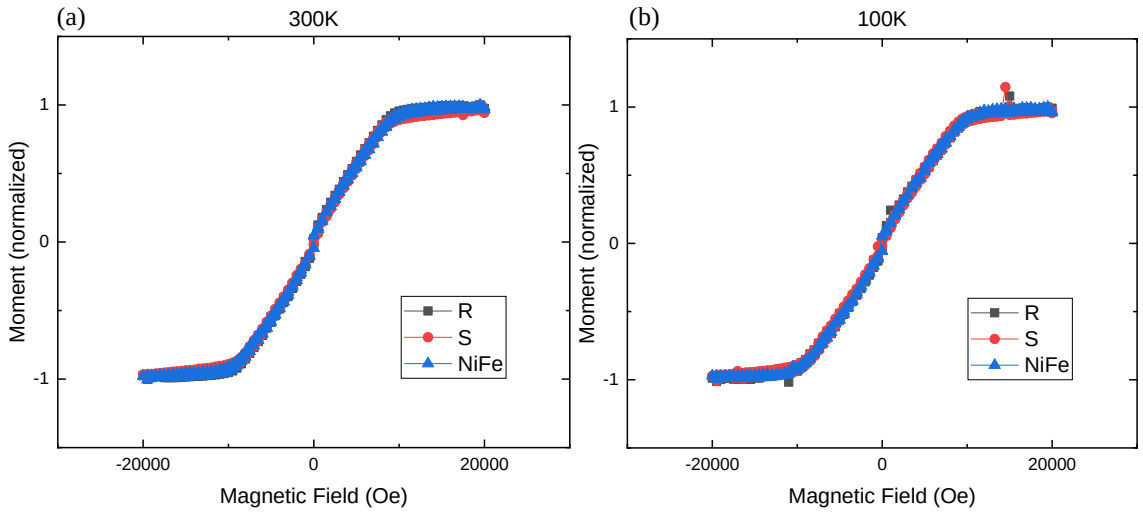

Fig. S13| The measured *M* vs. *H* loops along with the out-of-plane field direction measured in the control sample (NiFe/Cu/Si) and R/S STT devices (NiFe/Cu/(*R*(*S*)-(MePEA)$_2$PbI$_4$)/Si) at T = 300K (**a**) and 100K (**b**). The magnetic moment is normalized at the value of *H* = 20000 Oe.

After subtracting a linear background signal that corresponds to paramagnetic or diamagnetic contributions from the Si substrate, sample holder, and chiral-HOIPs, these data are normalized for the purpose of comparison among samples. The results clearly show that the easy axis of the NiFe film is indeed along with the in-plane direction for all the three samples as that in a typical NiFe film. There is no difference in the *M* vs. *H* loops between the chiral *R*(*S*) devices and the control NiFe sample. Due to the subtle difference in the sample surface roughness (shown in **Fig. S3**), there is a slight variation of the coercive fields between the control sample and the chiral devices. However, at room temperature this difference is only within 5 ± 4 Oe with an uncertainty caused by the sweeping field step, which is negligible compared to the minimum external magnetic field we used in this work for magnetic dynamics, *i.e.*, *H* > 500 Oe. When the sample is subjected to an external field strength larger than 500 Oe, the magnetic moments are the same for all the three samples. Since the shape anisotropy is the main source of magnetic anisotropy for these films, the total magnetization can be deduced from the saturation magnetic field in the out-of-plane *M(H)* loop measurements (**Fig. S13)**, which is $\mu_0 M_s = 1T$ for all three samples as expected for a typical NiFe film.

Therefore, we can safely conclude that the magnetization dynamics of the NiFe film in our work is the same in all three samples within the magnetic field range we applied in this work. There were reports showing that magnetic anisotropy of a ferromagnetic layer may be changed because of an interfacial magnetic proximity effect between chiral molecules and ferromagnetic layer. But in all our STT device configurations, the NiFe layer is well-separated from the chiral-HOIP layer owing to the 50nm-thick Cu spacer layer. Thus, the magnetic anisotropy of the top NiFe layer remains unchanged.

IV.2. Magnetization precession measurements on the NiFe/Cu/SiO_2/Si control sample: comparison between with and without external field

To show the difference between the ferromagnetic resonance magnetization precession signal and the thermally-driven demagnetization signal in NiFe, we measured the same control sample with and without external fields. The sample configuration is the same as described in the main text: NiFe (15 nm)/Cu (50 nm)/SiO_2 (300 nm)/Si. **Figure S14** shows the difference. Without external field, there is a demagnetization process with a time scale on the order of 1 ps followed by a slow recovery of magnetization with the time scale on the order of 2000 ps. The random thermal fluctuation induced change of magnetization direction determines the signals after 2000 ps, without any clear oscillating feature. With an external field, the demagnetization signal is followed by a damped-sine-wave oscillation, i.e., the magnetization precession, with the frequency that can be well-described by the Landau-Lifshitz-Gilbert (LLG) equation.[16] After the amplitude of precession is damped after 2 ns, the signals are the same as the without field ones due to the random thermal fluctuations.

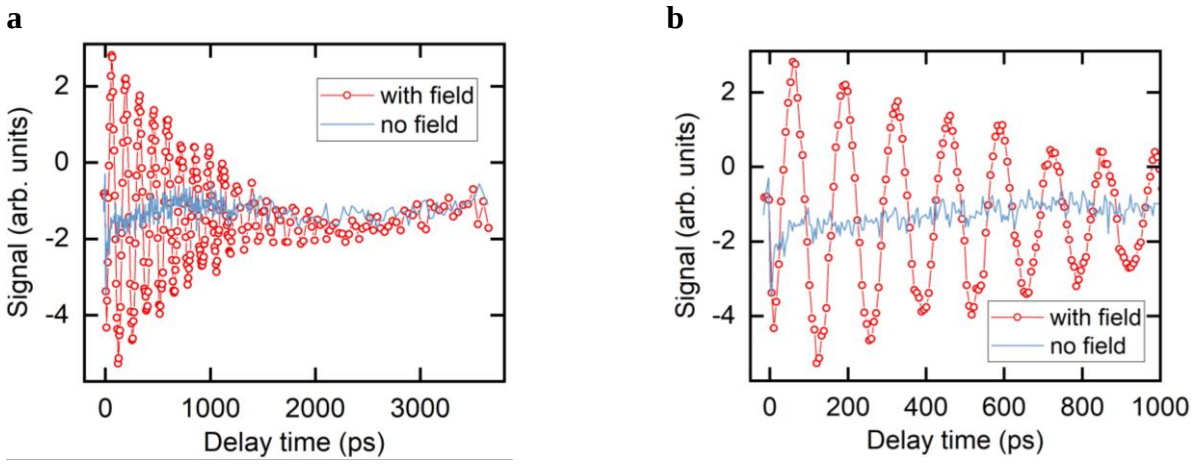

Fig. S14| Magnetization precession measurements on the NiFe/Cu/SiO2/Si control sample using the 10x objective lens (Gaussian spot size ≈6 microns), 32 mW effective incident pump and probe laser power, and with 270 mT external field applied at 20 degrees from the surface normal direction. In comparison, the measurement result without field is also shown. **a,** Full time scale with delay time from 0 to 3600 ps. **b,** Zoom-in time scale with delay time from 0 to 1000 ps.

V. FIELD AND TEMPERATURE DEPENDENCE OF SPIN ACCUMULATION AND SPIN TRANSFER TORQUE SIGNAL

V.1. Measurement results of spin accumulation on the Cu surface in Cu/(*S*-MePEA)$_2$PbI$_4$ /Si sample with varying external fields

To check whether the spin current in the Cu layer depends on the external fields or not, we measured the external field dependence of the spin accumulation signals in the Cu of the Cu/(*S*-MePEA)$_2$PbI$_4$ /Si sample. To enhance the signal to noise ratio, we have used a slightly higher power intensity by using the 20x objective lens. **Figure S15a** shows that the phase of the signal does not change with the fields and the amplitude of the oscillation varies with the external field, with the selected data overlapped in **Fig. S15b**. Because the spin accumulation on the Cu surface is due to the spin current and the measurement is in the polar-MOKE configuration, we assume that the change in the amplitude of the oscillation originates from the change of magnitude in the out-of-plane component of the spin current (J_{sz}).

We analyzed the spin accumulation data in the Cu/(*S*-(MePEA)$_2$PbI$_4$) sample using two different approaches: (1) Fast Fourier transform (FFT) fitting (see **Fig. S15c**): we performed FFT to identify the main frequency peak, and fitted the time-domain signal using the FFT-analyzed frequency. Error bars were provided based on the goodness of fit. (2) Direct reading (see **Fig. S15d**): we directly found the peaks and valleys and averaged the amplitudes of each peak. Statistical error bars were provided based on the variations of all the amplitudes of individual peaks. Moreover, to further validate our previous measurements, we also re-measured the sample (labeled as "2nd") under a large range of external fields. The maximum field strength is doubled from ~±200 mT to ~±400 mT in the new measurements. **Figures S15e** and **S15f** show the FFT fitting and direct reading amplitudes of both "1st" and "2nd" measurements, respectively. We conclude that the field dependence of the out-of-plane spin accumulation signals is weak. For instance, there is less than ~30% increase in amplitude when the external field increases from 0 mT to ~+300 mT. This change is much smaller compared to that in the in-plane polarization component of the spin current (see **Fig. 4d** in the main text).

The CPASS effect does not require an external magnetic field, but the magnetic field could enhance the breaking of time-reversal symmetry in addition to the temperature gradient and thus enhance the CPASS effect. This effect has been predicted by one of our co-authors.[17] We found that this enhancement effect is mainly on the ***in-plane polarization*** of the spin current, as shown in the main text **Fig. 4d**, not in the out-of-plane polarization of the spin current, which is quantified by the spin accumulation on the Cu/HOIP films via the polar TR-MOKE measurements, with the results shown in the **Fig. S15**. A future theoretical work is needed to elucidate the fundamental mechanism for this magnetic-field dependence observation.

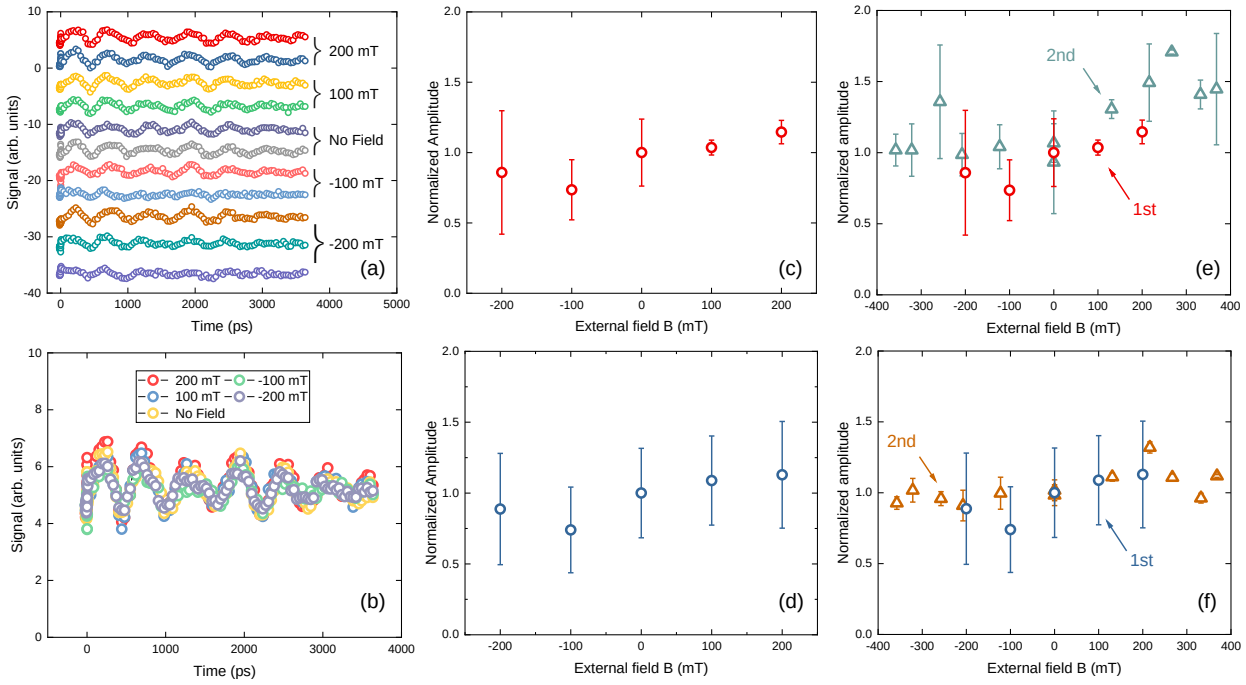

Fig. S15| Field dependence of spin accumulation signals measured in the Cu/(*S*-(MePEA)$_2$PbI$_4$) sample. Obtained raw data under a field strength ranging from -200 mT to +200 mT that is shifted vertically (**a**) and overlapped (**b**) for better comparison. Oscillation amplitude obtained by FFT fitting (**c**) and by direct reading (**d**). Fitted oscillation amplitude obtained by FTT and direct reading are respectively shown in (**e**) and (**f**), including both 1st (circles) and 2nd (triangles) measurements under a larger range of external fields ranging from -400 mT to +400 mT. Data are presented as mean values ± standard deviation in **(c)-(f)**.

V.2. Temperature dependence of the transient MOKE signals in NiFe/Cu/(*S*-MePEA)$_2$PbI$_4$ /Si sample

Figure S16a shows the TR-MOKE signal as a function of the environmental temperature on the NiFe (15 nm)/Cu (50 nm)/(*S*-MePEA)$_2$PbI$_4$ (150 nm)/Si sample, without applying any external magnetic field. This is achieved by carrying out the measurements in a cryostat (ARS-DMX-20-OM) with optical access. The vacuum pressure is kept below at least 10^{-6} mbar during the measurements. We analyzed the temperature dependence data and summarized the dependence of the frequency, phase, and amplitude on the temperature. **Figure S16b-e** show an increase of oscillation frequency, a constantly shifting phase, and an increased oscillation amplitude with a decreasing temperature from 300 K to 100 K. The signal due to the CPASS effect is strong at both room-temperature and low temperatures, which means this effect is temperature-robust.

The complicated interplays of chiral phonons population, chiral phonon transport (i.e., propagation and scattering), chiral phonon-spin interaction, and spin transport in the metallic layer as a function of temperature determine that the environmental temperature dependence of the CPASS effect is NOT a simple monotonic relation in contrast to that of other thermal activated phenomena. Our observations at a **thermal non-equilibrium condition** due to the applied thermal gradient should be clearly distinguished from the temperature-dependent signals in most CISS-

related reports in chiral materials **at the thermal equilibrium condition** that were attributed to the thermally activated magnetic proximity effect[18] or coupling mediated by thermally activated conduction electrons between paramagnetic elements embedded in the chiral materials[19].

Specifically, there are the following four main factors (at least) that will affect the CPASS effect as a function of environment temperature:

(i) ***Chiral phonon population***. Generally, phonon population follows the Bose-Einstein distribution, which varies dramatically with the environmental temperature. Certain chiral phonons with a high vibrational frequency might not be excited at a lower temperature, leading to a reduction of the generation of chiral phonons, i.e., the CPASS effect might be **reduced** at low temperatures.

(ii) ***Chiral phonon scattering***. The propagation of the chiral phonons relies on group velocities of the phonon modes and the scattering rates with other chiral phonons that are strongly temperature dependent. Particularly, the phonon scattering rate is much lower at a lower temperature. In some extreme cases, the generated chiral phonons could transmit ballistically to the interface at a lower temperature, without experiencing scattering. Namely, the CPASS effect would **increase** at low temperatures because of the longer phonon propagation length.

(iii) ***Chiral phonon-spin interaction*** across the Cu/HOIP interface, which determines the spin-mixing conductance that is a conversion efficiency between the angular momentum of chiral phonons and spins in the Cu layer. This conversion efficiency may be highly dependent on the temperature. If we take a similar conversion efficiency derived from the regular spin Seebeck effect in ferromagnetic semiconductor as an example, C. M. Jaworski *et al*. reported the SSE-induced conversion effect exhibits a sharp increase when the temperature is decreased[20]. In this case, the CPASS effect may also **increase** at low temperatures.

(iv) ***Spin relaxation time*** and ***spin diffusion length*** in the metallic Cu layer on top of chiral-HOIP will increase at a lower temperature, resulting in an increase of spin accumulation on the surface of the Cu layer probed by polar MOKE technique. Under this condition, the CPASS effect will **increase** at low temperatures.

With the listed four factors, we want to point out that the phonon transport in ***chiral hybrid organic-inorganic perovskites*** (chiral-HOIPs) may play a dominant role in the temperature-dependent data since the spin Seebeck effect is directly proportional to the applied thermal gradient across the sample. Thermal conductivity k is a thermophysical property that directly and only depends on the (i) phonon population and (ii) phonon propagation in a specific material. For instance, the thermal conductivity of a crystalline material (e.g., Si) usually shows a strong temperature dependence due to the competition between an increased phonon population and an increased phonon scattering rate with increasing temperature. However, such a strong temperature dependence does not always appear in other complex crystals and HOIPs and their derivations. One experimental evidence is a recent study[21] on the comparison between temperature dependences of thermal conductivity in $CH_3NH_3PbBr_3$ and $CsPbBr_3$. They demonstrated that the temperature dependence becomes very weak in the range of 100 K to 300 K in $CH_3NH_3PbBr_3$ compared to its inorganic counterpart, $CsPbBr_3$. This different temperature dependence was attributed to a synergic effect of accelerated organic cation dynamics in $CH_3NH_3PbBr_3$ at low temperature and the lower phonon group velocity but higher phonon Umklapp scattering rate at high temperature.

Studying competitions among these factors are more complicated beyond the current scope of this work that reports the CPASS effect at room temperature. For example, at lower

temperatures there will be fewer excited phonons which reduces the total number of possible chiral phonons that may transfer angular momentum. Meanwhile, these chiral phonons will experience fewer scattering events which will increase the probability of chiral phonons reaching the interface without many interruptions (elastic or inelastic scattering events). Moreover, the temperature dependence of the CPASS conversion efficiency between chiral phonons and spins remains unknown. Thus, the detected weak temperature dependent CPASS signal represents the overall result of competitions between four factors (at least) listed above.

In summary, further in-depth studies on the temperature dependence of the CPASS effect require significant modeling efforts from the communities to understand the chiral phonon modes and how they propagate and interact with spins in the specific materials at various temperatures. It would also greatly benefit from new experiments using a coherent excitation of chiral phonons in contrast to the incoherent excitation of phonons produced by the temperature gradient. Both the phonon modeling and future experimental work may provide a route to elucidate the fundamental physical picture of this weak temperature dependence.

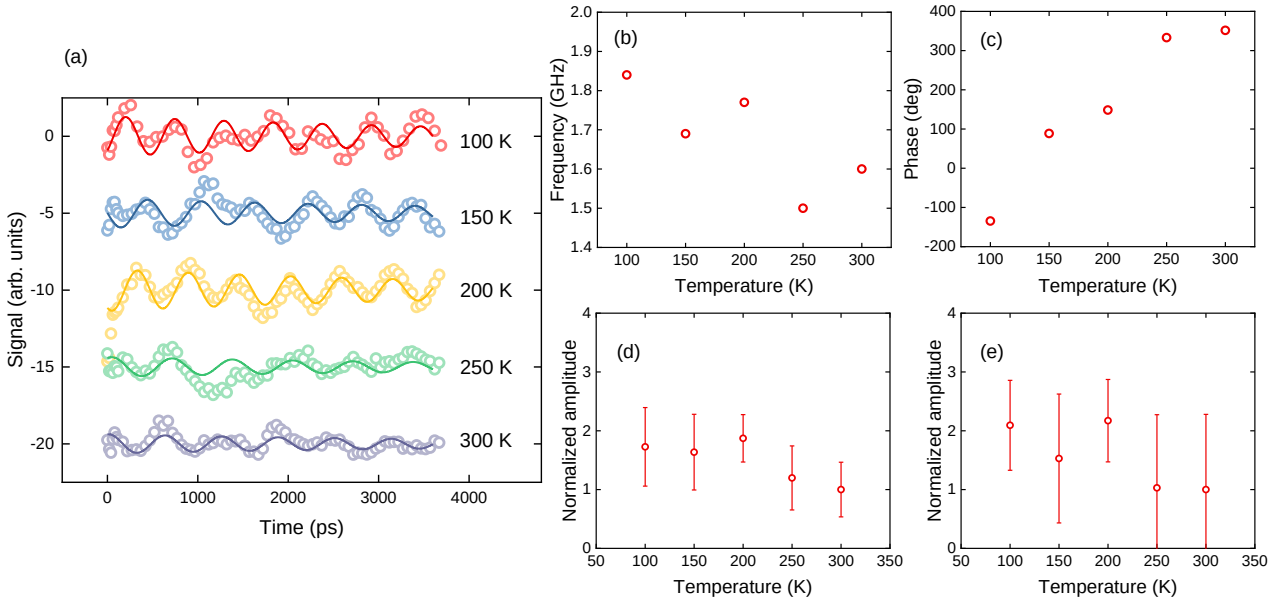

Fig. S16| Temperature dependence of the CPASS effect. a, The transient MOKE signal as a function of the environmental temperature on the NiFe/Cu/(*S*-MePEA)$_2$PbI$_4$/Si sample, without applying any external field. The experimental data (open circles) and the fitting results (solid lines) are shown. Raw data is shifted vertically for clarity. Analysis results on the oscillation frequency **(b)**, oscillation phase **(c)**, normalized oscillation amplitude analyzed using a direct method **(d)**, and normalized oscillation amplitude analyzed using the Fast Fourier Transform (FFT) method **(e)** with the fitting results shown in **(a)**. Data are presented as mean values ± standard deviation in **(d)** and **(e)**.

V.3. Analysis of the ferromagnetic resonance mode (the '*FMR mode*') with external field on the chiral and control samples

To understand the nature of the injected spin current into the ferromagnetic NiFe layer, we measured three samples with the same applied external field: the NiFe control sample (NiFe/Cu/SiO_2/Si), Chiral-S (NiFe/Cu/(*S*-MePEA)$_2PbI_4$/Si), and Chiral-R (NiFe/Cu/(*R*-MePEA)$_2PbI_4$/Si) samples. Because even the nominal angle of the external field is set as 20 degrees, the actual exact angle of external field is unknown with a potentially slight deviation, so we fitted the experimental data on the control sample to determine the exact angle. **Figure S17** shows that the exact angle of external field for the positive and negative field is 22.4° and 20.4°, respectively, which is close to the nominal value, 20°. Comparing the frequencies of the ferromagnetic resonance modes at the same external field in chiral samples, we found that there is no significant difference between the NiFe control sample and the chiral samples in terms of their frequencies of FMR modes. We can conclude that the field-like torque is negligible in this set of measurements. Thus we can conclude that the potential effective field from chiral phonons should be negligible in all our measurements.

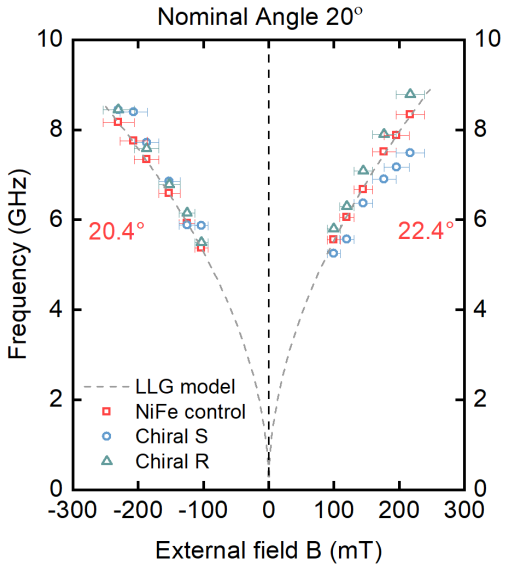

Fig. S17| Obtained FMR frequency as a function of the external field strength on the NiFe control sample (NiFe/Cu/SiO_2/Si), Chiral S (NiFe/Cu/(*S*-MePEA)$_2PbI_4$/Si), and Chiral R (NiFe/Cu/(*R*-MePEA)$_2PbI_4$/Si) samples, respectively. The measurement conditions are: 10x objective lens (Gaussian spot size ≈6 microns); the effective incident pump and probe laser power is fixed at 32 mW. An external magnetic field is applied along with a 20-degrees nominal angle from the surface normal direction. The dashed lines are fittings from the Kittel formula containing calculated field angles labeled in the figure. The error bars on the field strength are determined by assuming the uncertainty of the probe sensor position of the Gauss meter (which was used to determine the field strength during the experiments) is 0.5 mm. Data are presented as mean values ± standard deviation.

Figure S18 shows an expanded view (zoomed-in in the range of 0-1000 ps) of the main text **Fig. 3e and Fig. 3f**, which clearly shows the opposite phase when the magnetic field is reversed for the ***FMR mode***.

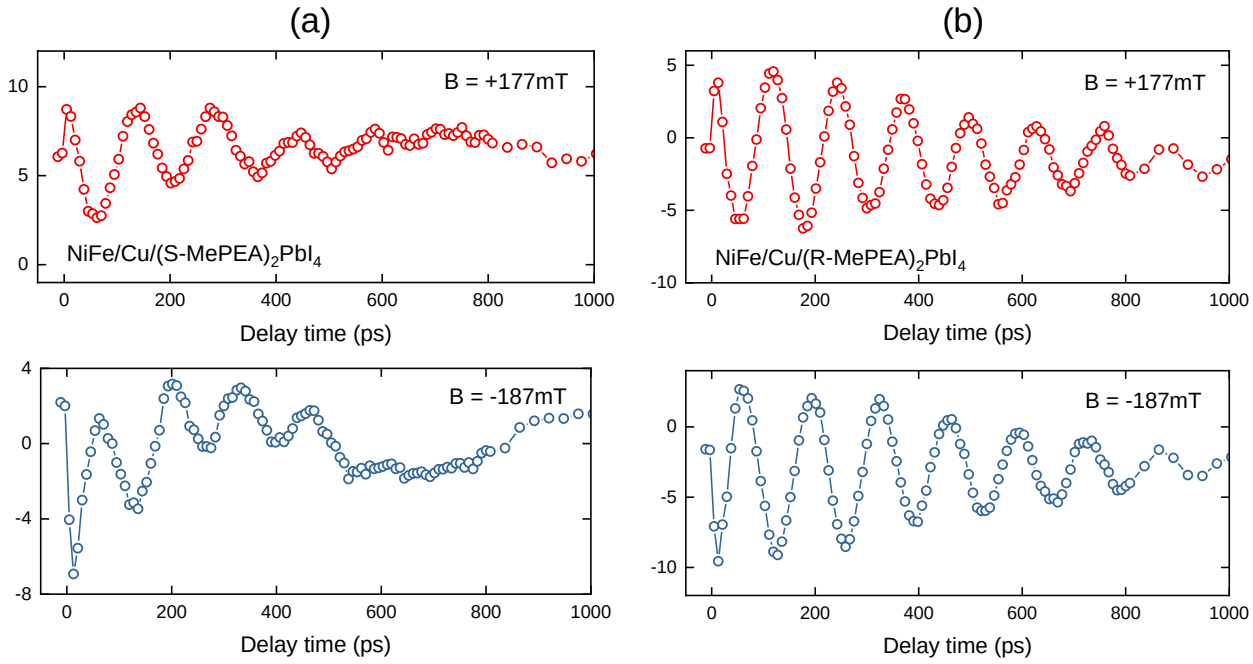

Fig. S18| The expanded view of the main text Fig. 3e and Fig. 3f that shows a zoomed-in view of the 0-1000 ps time delay. Transient Kerr rotation signals measured in the NiFe/Cu/(S-MePEA)$_2$PbI$_4$ **(a)**, and NiFe/Cu/(R-MePEA)$_2$PbI$_4$ **(b)** device while applying an external magnetic field at an angle of 70º with respect to the film plane (B ~ ±180 mT), respectively.

VI. SOLVING SPIN CURRENT DENSITY BY FITTING MULTIPLE TIME-RESOLVED EXPERIMENT DATA

VI.1. Analysis of oscillating modes (*FMR* and *STT* modes) in time-resolved polar MOKE measurement results and fitting the time-resolved data

For the polar MOKE measurements, the Kerr rotation angle is proportional to the projected magnetization in the out-of-plane, i.e., z-direction, which is M_z. The evolution of M_z in time t during precession appears as a decaying sinusoid, which can be expressed as

$$M_z(t) \propto \sin(2\pi ft + \varphi)\exp(-t/\tau), \quad \text{(Eq. S6)}$$

where f, φ, and τ are the resonance frequency, the oscillation phase, and the relaxation time of magnetization precession, respectively. For comparison, the thermal background from the raw TR-MOKE measurement data $\theta_K(t)$ was subtracted to obtain the pure precession signal, which oscillates sinusoidally at a decaying rate related to the damping. This involves fitting the data to the equation

$$\theta_K(t) = A + B\exp(-t/a) + C\sin(2\pi ft + \varphi)\exp(-t/\tau), \quad \text{(Eq. S7)}$$

and subtracting the thermal background

$$A + B\exp(-t/a), \quad \text{(Eq. S8)}$$

where A, B, and a are fitting constants. The constant C is the amplitude of oscillation. In our measurements, there are two oscillation modes, so the fitting equation is

$$\begin{aligned}\theta_K(t) = {} & A + B\exp(-t/a) + C_1\sin(2\pi f_1 t + \varphi_1)\exp(-t/\tau_1) \\ & + C_2\sin(2\pi f_2 t + \varphi_2)\exp(-t/\tau_2)\end{aligned}. \quad \text{(Eq. S9)}$$

In order to obtain the oscillation frequency f_1 and f_2 with a higher accuracy, the Fast Fourier Transformation (FFT) was also applied to identify the frequencies. Once the two frequencies are found, parameters such as τ_1, τ_2, C_1, and C_2 are fitted with a rough estimation. Then we used the Landau–Lifshitz–Gilbert-Slonczeswki (LLGS) equation to fit the exact shape and value of the experiment data, obtaining more accurate results of the parameters.

The Landau–Lifshitz–Gilbert-Slonczeswki (LLGS) equation incorporating spin transfer torque (STT) terms[16] is:

$$\frac{d\vec{m}(t)}{dt} = -\gamma\vec{m}(t)\times\vec{B} + \alpha\vec{m}(t)\times\frac{d\vec{m}(t)}{dt} + \frac{h\gamma}{4\pi eM_s d}\vec{m}(t)\times\left[\vec{m}(t)\times\overrightarrow{J_{s,z}}(t)\right], \quad \text{(Eq. S10)}$$

where $\vec{m}(t)$ and $\overrightarrow{J_{s,z}}(t)$ are the time-dependent unit vectors of the magnetization of the NiFe layer and the injected spin current density vector, respectively. In the main text, we simplified the notation for the spin current density because all the spin currents in our setup flow in the z direction. Here, we use the full notation where the subscript means the flow direction of the spin current, and the superscript means the polarization direction of the spin. The spin current density vector $\overrightarrow{J_{s,z}}(t)$ has three components, where $J^x_{s,z}, J^y_{s,z}, J^z_{s,z}$ represents the amplitude of the time-varying oscillation

at each polarization, respectively. $\vec{B}$ is the applied external magnetic field, γ is the gyromagnetic ratio, h is the Planck constant, α is the Gilbert damping constant. The third term on the right-hand side of the Eq. (S10) presents the damping-like STT contribution. M_s and d are the saturation magnetization and thickness of the NiFe layer, respectively. We used the values $\mu_0 M_s = 0.96$ T, $\alpha = 0.039$, $d = 15$ nm, $\gamma = 1.8 \times 10^{11}$ rad/(s · T) for the NiFe layer.[22] Here we assume the polarization efficiency is 100%, which means there is only one spin polarization vector direction at any given time *t*.

Figure S19 shows two important experimental observations besides what we have shown in the main text that enable us to rule out other possible spin current expressions and determine the spin current format. Figure S16a shows that the amplitude of the STT mode decreases with the increasing positive field strength whereas it increases with the increasing negative field strength. Figure S16b shows that the phases of the STT mode are very different at a relatively large external field strengths whereas the phases of the STT mode are similar at smaller field strengths.

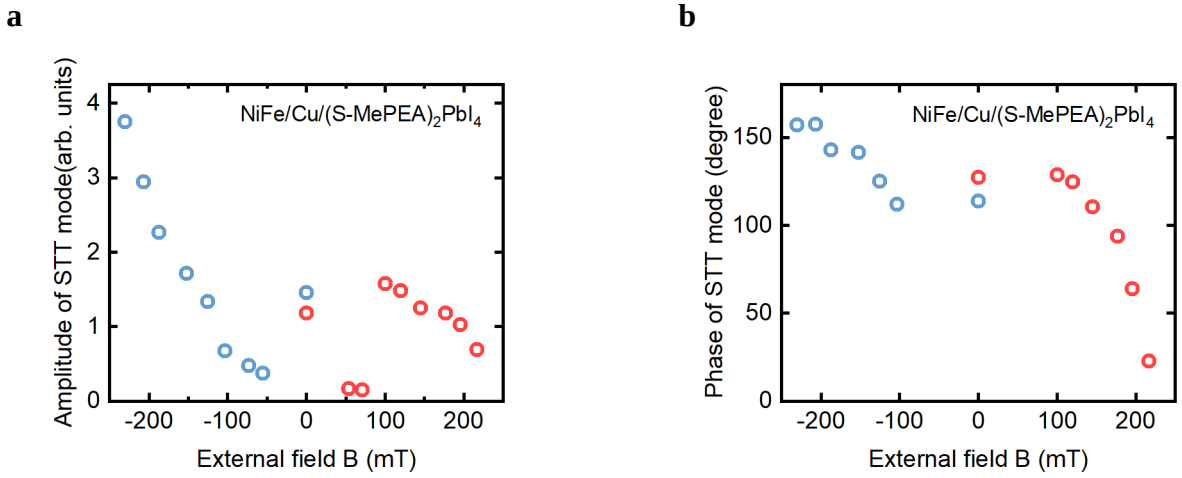

Fig. S19| Experimental observations of the dependence of applied external field on the STT mode. a, The amplitude of the STT mode. **b,** The phase of the STT mode.

The terms with the spin current are very important in the LLGS equation and the format of the spin current is unknown. Therefore, we have used seven reasonable expressions for the spin current (See **Table S4**) and found that only the 7th expression matches with the experimental observations. **Figure S20** shows the predicted signals using the spin current expression 1-6, which do not match with the experimental observations (see the figures in the main text and in **Fig. S19**).

Table S4. Possible spin current expressions.

ID	Spin current expression	Comments
1	$\vec{J}_{s,z}(t) = J^{z}_{s,z}\vec{k}$	No oscillation of a STT mode
2	$\vec{J}_{s,z}(t) = J^{z}_{s,z}\cos(\omega t)\vec{k}$	The field dependent amplitude of the STT mode has a very different trend with the experiment data; no field dependent phase shift of the STT mode
3	$\vec{J}_{s,z}(t) = J^{x}_{s,z}\sin(\omega t)\vec{i}$	No oscillation of the STT mode at zero field
4	$\vec{J}_{s,z}(t) = J^{x}_{s,z}\sin(\omega t)\vec{i} + J^{z}_{s,z}\vec{k}$	Same as 3
5	$\vec{J}_{s,z}(t) = J^{x}_{s,z}\vec{i} + J^{z}_{s,z}\cos(\omega t)\vec{k}$	Same as 2
6	$\vec{J}_{s,z}(t) = J_{s,z}\sin(\omega t)\vec{i} + J_{s,z}\cos(\omega t)\vec{k}$	The field dependent amplitude of the STT mode has a very different trend with the experiment data
7	$\vec{J}_{s,z}(t) = J^{x}_{s,z}\sin(\omega t)\vec{i} + J^{z}_{s,z}\cos(\omega t)\vec{k}$	Match with the experiment data with a field dependent spin current

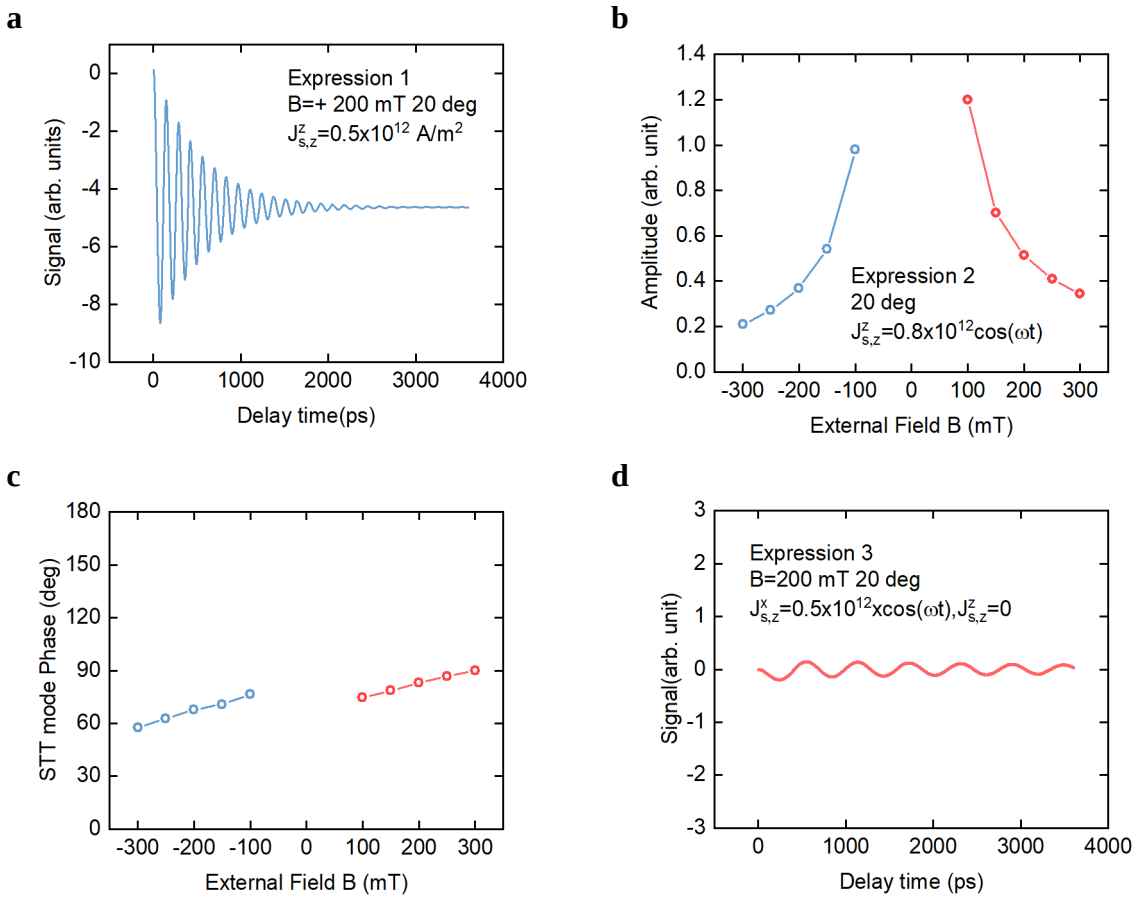

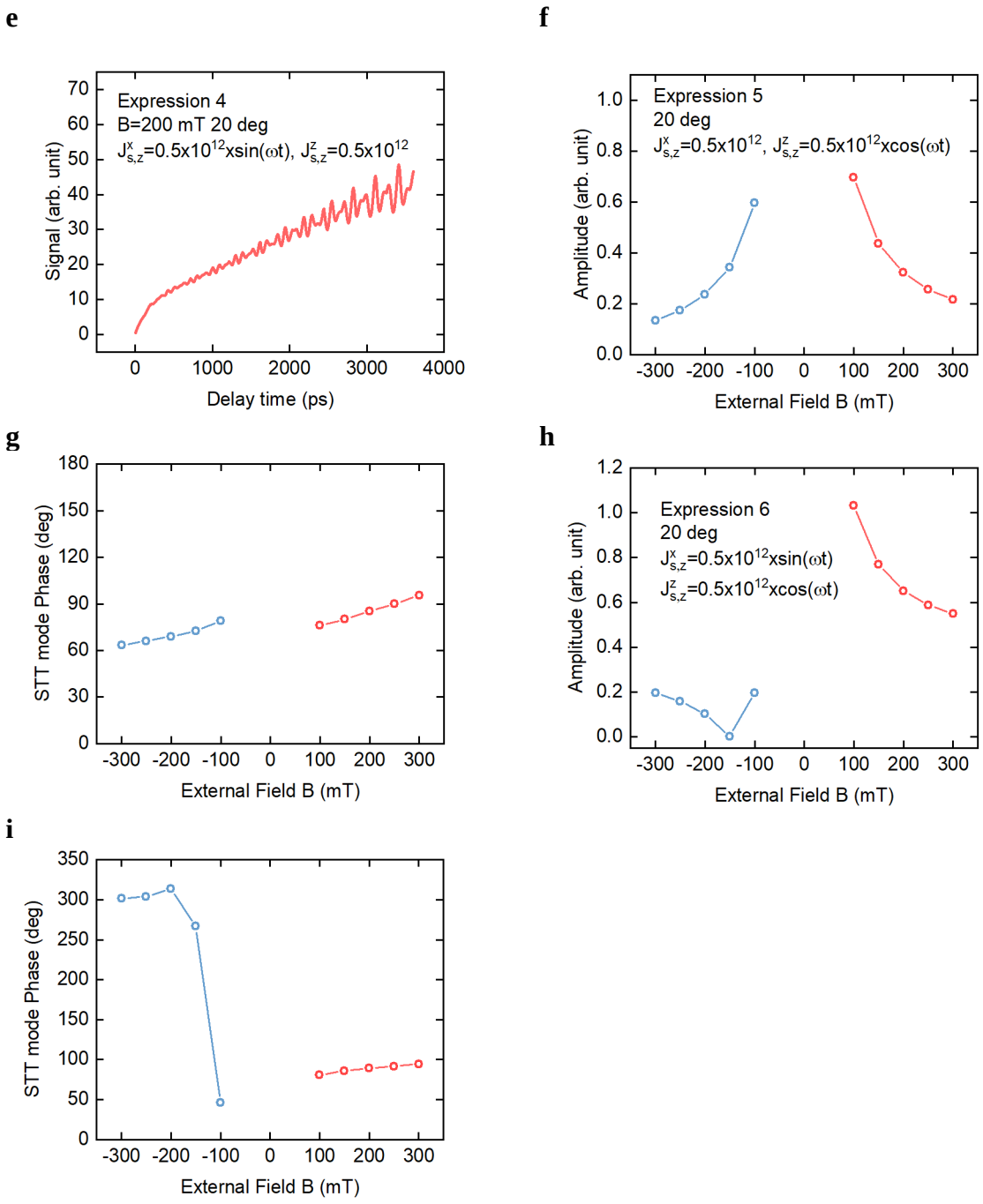

Fig. S20| The inconsistency with the experimental data if using the other six spin current expressions: expression 1 **(a)**; expression 2 **(b)** & **(c)**; expression 3 **(d)**; expression 4 **(e)**; expression 5 **(f)** & **(g)**; expression 6 **(h)** & **(i)**. The detailed reasons are commented in Table S4.

Examples of the fitted data are shown in main text **Fig. 4**. From the fitting, we can extract the magnitude of the spin current density (see the main text), the frequency of FMR mode (see **Fig. S17**), and the frequency of the STT mode. **Figure S21** shows the frequency of the STT mode and

their dependence on the applied external fields. It remains as a future investigation on why the frequency of STT mode will depend on the external field.

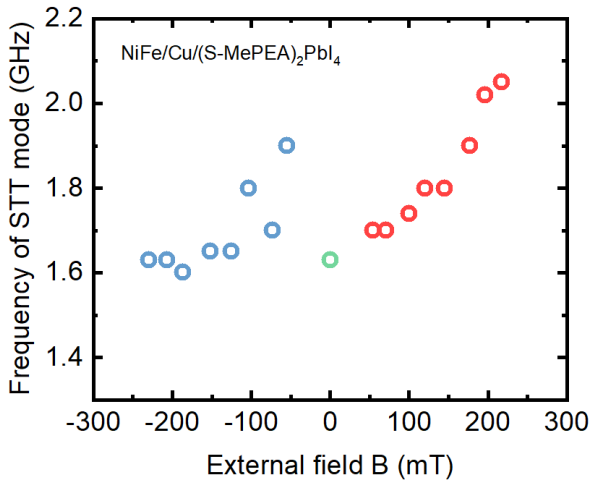

Fig. S21| The oscillation frequency of STT mode and its dependence on the applied external fields.

To show how the spin current density oscillates in the three-dimensional space, we have uploaded an animation in the **Supplementary Video 1**, where the time-dependent spin current is visualized with different applied external magnetic fields.

VII. CPASS COEFFICIENT

VII.1. Calculation of the conversion coefficient in the literature work

In the main text, we define the energy conversion coefficient in the CPASS effect as:

$$S_{CPASS} \equiv \frac{|\vec{J}_s|}{|\nabla T|}, \qquad \text{(Eq. S11)}$$

where $|\nabla T|$ is the temperature gradient generated across the sample structure induced by ultrafast laser heating. The unit of this coefficient is $\mathrm{A}/(\mathrm{K}\cdot\mathrm{m})$. To enable a fair comparison, we calculated the thermal-electron spin conversion coefficient between the spin current density and temperature gradient in spin Seebeck effect or spin-dependent Seebeck effect from the values provided in the literature, with the same unit.

Because most of the literature we found does not have the full list of parameters, we list the literature work that has a full list of parameters needed to calculate the spin current density and temperature gradient. To calculate the spin current density from the voltage that commonly reported in these publications, we derived an equation considering a general device configuration shown in **Fig. S22**. NM or the subscript *N* means the normal metal, which is usually Pt. FM or the

subscript F represents the magnetic material. V is the reported voltage. w and l are the lengths along and perpendicular to the voltage drop direction, respectively.

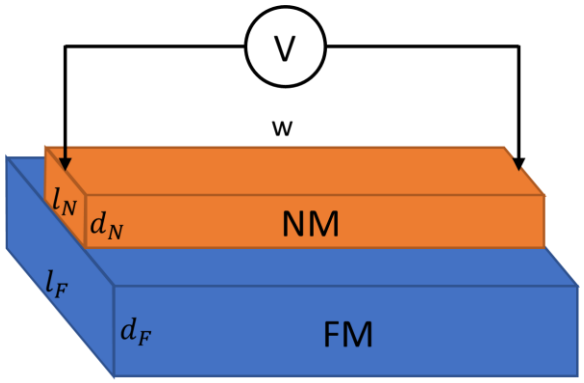

Fig. S22| The general device configuration reported in the literature to measure the spin Seebeck effect. NM or the subscript N means the normal metal, which is usually Pt. FM or the subscript F represents the magnetic material. V is the reported voltage. w and l are the lengths along and perpendicular to the voltage drop direction, respectively.

To calculate the spin current density injected into the normal metal (e.g., Pt), we derived the following equation to extract the spin current density $|\vec{J}_s|$,

$$|\vec{J}_s| = \frac{V_{ISHE}(l_N d_N \sigma_N + l_F d_F \sigma_F)}{w l_N \theta_{SHE} \lambda_N \tanh(d_N/2\lambda_N)}, \quad \text{(Eq. S12)}$$

where V_{ISHE} is the inverse spin Hall effect voltage that is usually measured in the literature. λ and σ are the spin diffusion length and electrical conductivity of the layer, respectively. θ_{SHE} is the spin Hall angle in the normal metal. **Table S5** lists the reported device parameters and measurement results for the Seebeck effects found in the literature. Note that if Pt is used as the normal metal, $\theta_{SHE} = 0.037$ and $\lambda_N = 10$ nm .**Table S6** shows the calculated thermal-electron spin conversion coefficient for the corresponding literature work.

Table S5. The reported device parameters and measurement results for the spin Seebeck and spin-dependent Seebeck effects in the literature.

ID	*Magnetic layer*	*Normal metal*	w *(mm)*	d_N *(nm)*	l_N *(mm)*	σ_N $(\Omega m)^{-1}$	d_F *(mm)*	l_F *(mm)*	σ_F $(\Omega m)^{-1}$	V_{ISHE} *(μV)*
1	$Ni_{81}Fe_{19}$	Pt	3	10	0.1	2e6	2e-5	0.1	1.5e6	0.5
2	Co/Ni	-	-	-	-	-	-	-	-	-
3	$LaY_2Fe_5O_{12}$	Pt	4	15	0.1	2e6	3.9e-3	8	2e-5	1.3
4	YIG	Pt	6	10	2	2e6	1	2	2e-5	37
5	YIG	Pt	6	15	0.5	2e6	1	2	2e-5	15
6	YIG	Pt	7	10	3	2e6	1	3	2e-5	10
7	YIG	Pt	6	10	2	2e6	1	2	2e-5	6
8	YIG	Pt	10	6	2.3	2e6	8e-3	2.3	2e-5	10
9	YIG	Pt	5	10	2	2e6	6e-5	2	2e-5	2.5
10	NFO	-	-	-	-	-	-	-	-	-
11	Cr_2O_3	Pt	4	10	2	2e6	0.5	2	0.1	1.5
12	GaMnAs	Pt	4	20	0.25	2e6	3e-5	10	1e4	0.7

Table S6. The thermal-electron spin conversion coefficient $J_s/\nabla T$ for the literature work.

ID	*Reference No.*	*Magnetic layer*	$\lvert\vec{J_s}\rvert$ (A/m^2)	$\lvert\nabla T\rvert$ (K/m)	$\lvert\vec{J_s}\rvert/\lvert\nabla T\rvert$ $(A/(m\cdot K))$
1	**23**	$Ni_{81}Fe_{19}$	4.87e4	2500	19.50
2	**2**	Co/Ni	9.77e10	1.17e10	8.347
3	**24**	$LaY_2Fe_5O_{12}$	4.15e4	2500	16.60
4	**25**	YIG	7.21e5	3e4	24.04
5	**26**	YIG	3.19e5	2.5e4	12.77
6	**27**	YIG	1.67e5	4000	41.78
7	**28**	YIG	1.17e5	3e4	3.899
8	**29**	YIG	1.11e5	3e4	3.711
9	**30**	YIG	5.85e4	4285.7	13.65
10	**31**	NFO	-	-	43.48
11	**32**	Cr_2O_3	4.40e4	3e4	1.466
12	**20**	GaMnAs	3.23e4	30	538.2

References

1 Danan, H., Herr, A. & Meyer, A. J. P. New Determinations of the Saturation Magnetization of Nickel and Iron. *J. Appl. Phys.* **39**, 669-670(1968).

2 Choi, G.-M., Moon, C.-H., Min, B.-C., Lee, K.-J. & Cahill, D. G. Thermal spin-transfer torque driven by the spin-dependent Seebeck effect in metallic spin-valves. *Nat. Phys.* **11**, 576-581(2015).

3 Jiang, P., Qian, X. & Yang, R. Tutorial: Time-domain thermoreflectance (TDTR) for thermal property characterization of bulk and thin film materials. *J. Appl. Phys.* **124**, 161103(2018).

4 Cahill, D. G. Analysis of heat flow in layered structures for time-domain thermoreflectance. *Rev. Sci. Instrum.* **75**, 5119-5122(2004).

5 Feser, J. P., Liu, J. & Cahill, D. G. Pump-probe measurements of the thermal conductivity tensor for materials lacking in-plane symmetry. *Rev. Sci. Instrum.* **85**, 104903(2014).

6 Liu, J. *et al.* Ultralow Thermal Conductivity of Atomic/Molecular Layer-Deposited Hybrid Organic–Inorganic Zincone Thin Films. *Nano Lett.* **13**, 5594-5599(2013).

7 Liu, J. *et al.* Simultaneous measurement of thermal conductivity and heat capacity of bulk and thin film materials using frequency-dependent transient thermoreflectance method. *Rev. Sci. Instrum.* **84**, 034902(2013).

8 Liu, J. *et al.* Thermal Conductivity and Elastic Constants of PEDOT:PSS with High Electrical Conductivity. *Macromolecules* **48**, 585-591(2015).

9 CRC handbook of chemistry and physics. (1977).

10 Lugo, J. M. & Oliva, A. I. Thermal Diffusivity and Thermal Conductivity of Copper Thin Films at Ambient Conditions. *J. Thermophys Heat Transfer* **30**, 481-489(2016).

11 Assael, M. J., Botsios, S., Gialou, K. & Metaxa, I. N. Thermal Conductivity of Polymethyl Methacrylate (PMMA) and Borosilicate Crown Glass BK7. *Int. J. Thermophys.* **26**, 1595-1605(2005).

12 Putnam, S. A., Cahill, D. G., Ash, B. J. & Schadler, L. S. High-precision thermal conductivity measurements as a probe of polymer/nanoparticle interfaces. *J. Appl. Phys.* **94**, 6785-6788(2003).

13 Zhou, J., Li, N. & Yang, R. An electrohydrodynamics model for non-equilibrium electron and phonon transport in metal films after ultra-short pulse laser heating. *Eur. Phys. J. B* **88**, 156(2015).

14 Tong, Z., Li, S., Ruan, X. & Bao, H. Comprehensive first-principles analysis of phonon thermal conductivity and electron-phonon coupling in different metals. *Phys. Rev. B* **100**, 144306(2019).

15 Schulz, L. G. The Optical Constants of Silver, Gold, Copper, and Aluminum. I. The Absorption Coefficient k. *J. Opt. Soc. Am.* **44**, 357-362(1954).

16 Brataas, A., Kent, A. D. & Ohno, H. Current-induced torques in magnetic materials. *Nat. Mater.* **11**, 372-381(2012).

17 Zhang, L. & Niu, Q. Angular Momentum of Phonons and the Einstein--de Haas Effect. *Phys. Rev. Lett.* **112**, 085503(2014).

18 Kondou, K. *et al.* Chirality-Induced Magnetoresistance Due to Thermally Driven Spin Polarization. *Journal of the American Chemical Society* **144**, 7302-7307(2022).

19 Mondal, A. K. *et al.* Long-Range Spin-Selective Transport in Chiral Metal–Organic Crystals with Temperature-Activated Magnetization. *ACS Nano* **14**, 16624-16633(2020).

20 Jaworski, C. M. *et al.* Observation of the spin-Seebeck effect in a ferromagnetic semiconductor. *Nat. Mater.* **9**, 898-903(2010).
21 Wang, Y. *et al.* Cation Dynamics Governed Thermal Properties of Lead Halide Perovskite Nanowires. *Nano Lett.* **18**, 2772-2779(2018).
22 Vetter, E. *et al.* Tuning of spin-orbit coupling in metal-free conjugated polymers by structural conformation. *Phys. Rev. Mater.* **4**, 085603(2020).
23 Uchida, K. *et al.* Long-range spin Seebeck effect and acoustic spin pumping. *Nat. Mater.* **10**, 737-741(2011).
24 Uchida, K. *et al.* Spin Seebeck insulator. *Nat. Mater.* **9**, 894-897(2010).
25 Uchida, K. *et al.* Longitudinal spin Seebeck effect: from fundamentals to applications. *J. Phys.: Condens. Matter* **26**, 343202(2014).
26 Uchida, K.-i. *et al.* Observation of longitudinal spin-Seebeck effect in magnetic insulators. *Appl. Phys. Lett.* **97**, 172505(2010).
27 Uchida, K.-i., Kikkawa, T., Miura, A., Shiomi, J. & Saitoh, E. Quantitative Temperature Dependence of Longitudinal Spin Seebeck Effect at High Temperatures. *Phys. Rev. X* **4**, 041023(2014).
28 Kikkawa, T. *et al.* Longitudinal Spin Seebeck Effect Free from the Proximity Nernst Effect. *Phys. Rev. Lett.* **110**, 067207(2013).
29 Rezende, S. M. *et al.* Magnon spin-current theory for the longitudinal spin-Seebeck effect. *Phys. Rev. B* **89**, 014416(2014).
30 Kirihara, A. *et al.* Spin-current-driven thermoelectric coating. *Nat. Mater.* **11**, 686-689(2012).
31 Kim, M. Y., Park, S. J., Kim, G.-Y., Choi, S.-Y. & Jin, H. Designing efficient spin Seebeck-based thermoelectric devices via simultaneous optimization of bulk and interface properties. *Energy Environ. Sci.* **14**, 3480-3491(2021).
32 Seki, S. *et al.* Thermal Generation of Spin Current in an Antiferromagnet. *Phys. Rev. Lett.* **115**, 266601(2015).